Journal of Microscopy, Vol. 232, Pt 1 2008, pp. 99–105
Received 20 December 2007; accepted 11 March 2008

Sub-100-nanometre resolution in total internal reflection fluorescence microscopy

M. BECK, M. ASCHWANDEN & A. STEMMER
Nanotechnology Group, Department of Mechanical and Process Engineering, ETH Zurich, Tannenstrasse 3, 8092 Zurich, Switzerland

Key words. Electro-active polymer (EAP), harmonic excitation light microscopy (HELM), high resolution, structured illumination, wide-field microscopy.

Summary

Combining total internal reflection fluorescence microscopy with structured illumination allows optical wide-field imaging with sub-100-nanometre resolution. We present a novel objective-launch set-up for standing wave illumination that takes advantage of a tunable transmission diffraction grating and transparent phase shifters actuated by electro-active polymers to control the excitation pattern in three dimensions. Image acquisition is completed in less than 1 s. To reconstruct the extended image spectrum, we apply a new apodization function that results in a lateral resolution of 89 nm for green emission wavelength.

Introduction

Fluorescence microscopy and highly specific labelling of molecules and molecular assemblies have become indispensable tools in cell biology (Taylor & Wang, 1980; Stephens & Allan, 2003). Total internal reflection fluorescence (TIRF) microscopy is the method of choice for observing structures and processes close to cell surfaces and adjacent to the cover slip or glass slide. Illuminating the specimen with an evanescent wave decaying exponentially in axial direction results in an essentially two-dimensional (2D) image without interference from regions deeper within the sample (Axelrod, 2001). However, for proper analysis, many structures and processes require lateral resolution better than 100 nm. To this end, the resolution of TIRF microscopy needs to be extended beyond the classical diffraction limit.

Among the established approaches in high-resolution light microscopy (for overviews, see Gustafsson, 1999; Garini *et al.*, 2005), structured illumination, as suggested by Lukosz & Marchand (1963) and later implemented in standard epi-fluorescence microscopy (Bailey *et al.*, 1993; Heintzmann & Cremer 1999; Frohn *et al.*, 2000; Gustafsson, 2000), is particularly well suited for TIRF microscopy since the spatial period of the standing wave illumination pattern can be further reduced in the higher refractive index material of the specimen support (Cragg & So, 2000; So *et al.*, 2001; Chung *et al.*, 2006, 2007). Taking advantage of the non-linear response of fluorophores in the saturation regime (Heintzmann *et al.*, 2002; Gustafsson, 2005), resolution may be improved down to several 10 nm. However, such procedures typically require long acquisition times and may suffer from increased photobleaching and phototoxicity, limiting their application to biological specimens. Hence a technique relying on linear fluorophore response is preferred. In this regime, harmonic excitation light microscopy (HELM), also referred to as standing wave microscopy (Frohn *et al.*, 2000; Gustafsson, 2000), has already proven a resolution enhancement by a factor of two in standard epi-fluorescence, approaching 100 nm in TIRF mode (Chung *et al.*, 2007).

Here, we present an easy-to-implement TIRF-HELM set-up achieving sub-100-nm resolution in large area images. In our set-up, tunable optical elements actuated by electro-active polymers (EAP) control a 2D standing wave illumination pattern. A tunable polymeric diffraction grating allows one to vary the spatial period and penetration depth of the excitation light in the object plane, and two adjustable polymeric phase plates shift the illumination pattern laterally. Raw data are processed in a robust algorithm with an apodization function adapted to the extended HELM passband. We demonstrate a full width at half maximum point resolution of 89 nm on fluorescent spheres and further illustrate the dramatic resolution increase on HeLa cells transfected with actin-GFP (green fluorescent protein).

Extended resolution

Lateral resolution of diffraction-limited optical systems amounts to $\delta = \lambda/2n\sin(\alpha_{ap})$, where λ is the excitation

Correspondence to: A. Stemmer. Tel: +41 44 632 4572; fax: +41 44 632 1278; e-mail: astemmer@ethz.ch

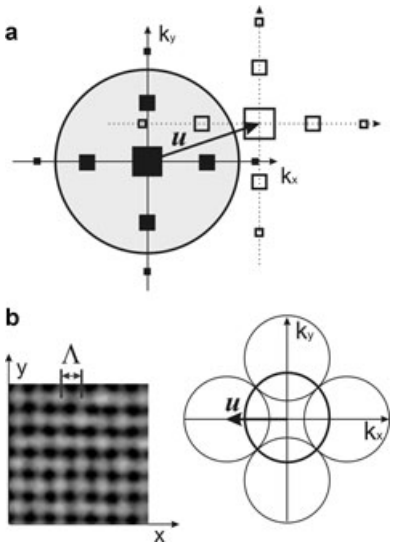

Fig. 1. (a) Structured illumination creates spectral copies (open squares) of the original spectrum (filled squares) shifted by the vector $\boldsymbol{u}$ out of the centre of the passband (shaded circle). Because of the shifted position of the spectral copies, higher spatial-frequency information (illustrated by smaller squares) is brought into the passband and contributes to image formation. (b) Two-dimensional illumination pattern of TIRF-HELM (left) and reconstructed extended passband (right).

wavelength in vacuum, n is the index of refraction and α_{ap} the half angle of the system's aperture. In frequency domain, this limit describes a circle centred at the origin of reciprocal space. Figure 1(a) illustrates a schematic image spectrum (filled squares) together with the passband of the microscope (shaded circle). Only spatial frequencies within the passband contribute to image formation, hence the smallest squares, representing high spatial frequency information, cannot be retrieved in classical light microscopy.

In HELM, high spatial frequency information is brought into the passband by illuminating the fluorescent sample with a standing wave pattern formed by two pairs of interfering laser beams. The emitted light ϕ is given by the density distribution of fluorophores ψ times the excitation intensity I, $\phi(x, y, z) = \psi(x, y, z)I(x, y, z)$. In TIRF-HELM, the excitation intensity is described by $I(x, y, z) = I_0 e^{-d/z}[2 + \cos(u_x x + \Delta\varphi_x) + \cos(u_y y + \Delta\varphi_y)]$, which is an evanescent wave in axial direction with a 2D cosine modulation laterally. The thickness of this structured light sheet is characterized by the penetration depth $d = (\mathrm{l}/4\pi)(n_1{}^2\sin^2\alpha - n_2{}^2)^{-1/2}$, where n_1 and n_2 represent the refractive indices of the cover slip and the specimen, respectively, and α is the angle of incidence of the excitation light at the glass-specimen interface.

Harmonic excitation results in additional copies of the image spectrum (open squares in Fig. 1(a)), shifted by the vector $u = 2\pi/\Lambda$, where $\Lambda = \lambda/(2n_1\sin\alpha)$ is the wavelength of the standing wave in the glass substrate. Because of this shift, higher spatial frequencies of the image spectrum (open squares) are brought into the passband of the microscope and can be detected, albeit at the wrong position in frequency space. For our 2D excitation pattern (Fig. 1(b)), the resulting fluorescence spectrum Φ is given by the linear combination of five spectral components, $\Phi(k_x, k_y) = 4A + e^{+i\Delta\varphi_x}B^+ + e^{-i\Delta\varphi_x}B^- + e^{+i\Delta\varphi_y}C^+ + e^{-i\Delta\varphi_y}C^-$. To reconstruct the extended object spectrum (Fig. 1b), we acquire a sequence of five raw images with the phase $(\Delta\varphi_x, \Delta\varphi_y)$ of the illumination pattern set to (0,0; $\pi/2$,0; π,0; 0,$\pi/2$; 0,π) and apply image arithmetic to determine the spectral components $A(k_x, k_y)$, $B^{\pm}(k_x, k_y)$, $C^{\pm}(k_x, k_y)$ as described by Frohn *et al.* (2000). Alternatively, the phase can be set to (0,0; $2\pi/3$,0; $4\pi/3$,0; 0,$2\pi/3$; 0,$4\pi/3$) to reduce bleaching effects in long-run experiments.

Materials and methods

Microscope set-up

Figure 2 illustrates schematically a cross-section of our telecentric TIRF-HELM set-up employing two pairs of interfering laser beams launched symmetrically around the objective's optical axis to form the 2D structured evanescent light field at the cover slip–specimen interface (for clarity, only one pair of interfering beams is shown). The excitation light is provided by a linearly polarized solid state laser (Sapphire 488–200, Coherent, $\lambda = 488$ nm, 1 W), delivered by a polarization maintaining single mode fibre and collimated to a diameter of 1.1 mm. A convex lens L_0 ($f = 100$ mm) is used to control the divergence of the Gaussian beam in the object plane. Shifting L_0 along the optical axis allows one to adjust the field of illumination w between 10 and 50 μm in diameter. An electrically tunable polymeric 2D sinusoidal phase grating (Aschwanden *et al.*, 2007) generates two orthogonal pairs of laser beams. To this end, only the first orders of diffraction ($\pm x$, $\pm y$) are retained, whereas a diaphragm blocks all other orders. The tunable grating is located in a secondary image plane and allows the diffraction angle to be varied, causing a proportional change of the illumination angle in the specimen plane. One beam of each pair ($-x$, $-y$) is directed through an electrically tunable polymeric phase plate to control the position of the illumination pattern in x- and y direction. To obtain two independently interfering beam pairs, half-wave plates turn the polarization of the $\pm x$ pair by 90°. As a result, both the $\pm x$ pair and the $\pm y$ pair are s-polarized and are not affected by phase aberrations at the edge of high NA objectives (Inoué & Kubota, 1958). In practice, we adjust the beam polarizations by turning the half-wave plates until the cross-interference pattern of (x, y) pairs disappears. The resulting 2D sinusoidal excitation pattern corresponds to a first-order projection of the grating.

The four beams enter the inverted microscope (Axiovert 200 M, Carl Zeiss, Jena, Germany) from the side via a coupling unit made of lens L_2 ($f = 30$ mm) and a 90° beam

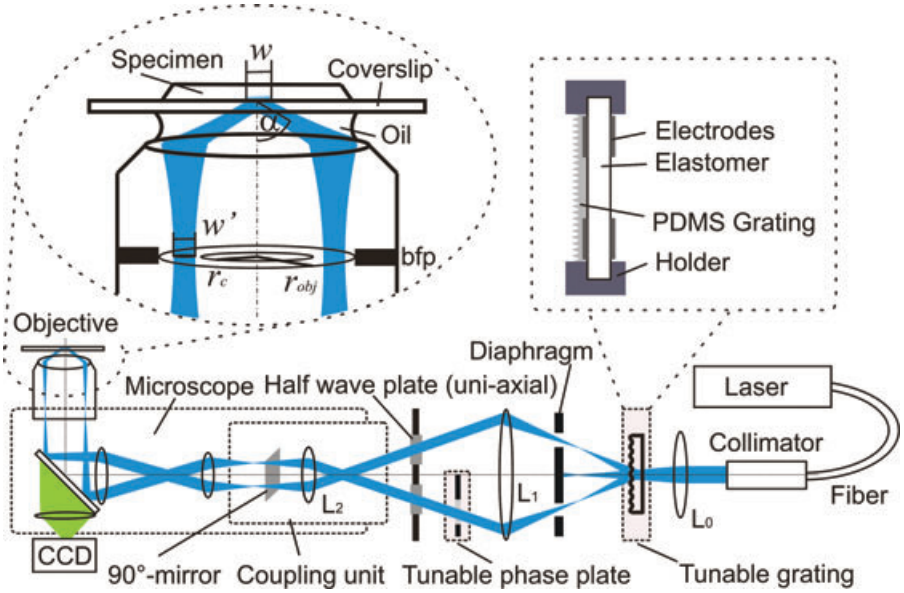

Fig. 2. Schematic cross-section of the TIRF-HELM set-up. An electrically tunable 2D sinusoidal phase grating, placed in a secondary image plane, and a diaphragm generate two orthogonal pairs of first-order diffracted beams (only one pair shown for clarity). Lenses L_1 and L_2 project the beam waists into the back focal plane (bfp) of the objective. The position of lens L_0 along the beam axis defines the field of illumination. Two electrically tunable phase plates, one per diffraction pair, shift the position of the standing wave illumination pattern in x- and y direction. One pair of diffracted beams is directed through $\lambda/2$ plates to obtain two pairs of orthogonally polarized beams. The left inset shows the beam configuration for total internal reflection; w and w' are the beam waist diameters in the object plane and the back focal plane, respectively, r_c is the critical radius for total internal reflection, r_{obj} is the radius of the objective exit pupil and α is the angle of illumination. The right inset is a cross-section through the polymeric tunable grating.

deflector (front surface silver-coated prism mirror, Thorlabs, Newton, NJ, USA). This coupling unit replaces the aperture diaphragm slider in the standard epi-illumination unit. L_1 ($f = 80$ mm) and L_2 ensure that the waists of the four beams are located on a ring in the back aperture plane of the objective (Fig. 2, left inset). To enable TIRF conditions for samples in aqueous medium, the width of the ring is given as $d = r_{obj}[1 - (n_w/n_{gl})]$, where r_{obj} is the radius of the objective exit pupil, $n_w = 1.33$ and $n_{gl} = 1.51$ are the refractive indices of water and glass, respectively. The inner radius of the ring, r_c, corresponds to the critical angle at the onset of total internal reflection. The beam waist w' depends on the desired field of illumination w and is given by $w' = f_{obj}\lambda/w\pi$, where f_{obj} is the objective focal length (Self, 1983). Using a Zeiss α Plan-Fluar 100×/1.45 oil objective and selecting the illumination field $w = 50$ μm requires a focal spot of $w' = 5.1$ μm for a ring width of $d = 300$ μm.

The fluorescence signal collected by the objective is separated from the excitation light by a dichromatic mirror and a bandpass filter (515–565 nm, Filter set 10, Carl Zeiss) and recorded with a cooled CCD camera (ORCA ERG, Hamamatsu).

Tunable grating and phase plate

The tunable 2D transmission grating is fabricated by micro-moulding as described by Aschwanden *et al.* (2007). A 1-mm-thick acrylic dielectric elastomer tape (VHB 4910, 3M) is pre-stretched (300% × 300%) to a final thickness of 62 μm and mounted on a PMMA frame (Fig. 2, right inset). Compliant carbon black ring electrodes are contact printed using a carbon black–coated poly(dimethylsiloxane) (PDMS) stamp. This structure forms the actuator. A 15-μm-thick PDMS film (Sylgard 184, 10:1 mixture, Dow Corning, Midland, MI, USA) is spin coated onto a 2D sinusoidal master grating (13500 lines/inch, RainbowSymphony, Reseda, CA, USA) and placed onto the dielectric elastomer actuator. After removing trapped air bubbles in vacuum and curing at 65°C, the grating master is peeled off from the thermally bonded PDMS layer. Applying a voltage of 4.5 kV, results in a lateral compression of the grating period by 7.5%. Diffraction efficiency into the first orders amounts to 28% and could be improved by adapting the groove height to blue light.

The tunable phase plate is built from just a pre-stretched (300% × 300%) dielectric elastomer film (VHB 4910, 3M) with contact printed compliant carbon black ring electrodes of 4 mm inner diameter and 1 mm width (Fig. 3(a)). Applying a voltage to the ring electrodes induces an electromechanical thickness strain between the electrodes that results in an increase in optical path length over the clear aperture, due to the incompressibility of the elastomer material. Increasing the applied voltage from 0 V to 3.7 kV covers a tuning range of 7 λ at 488 nm (Fig. 3(b)). An offset voltage of $U_0 = 2.5$ kV is applied

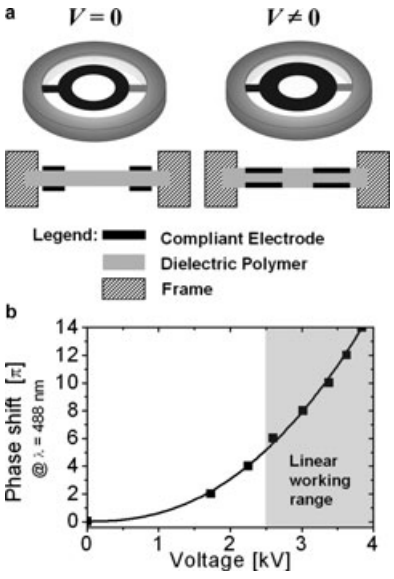

Fig. 3. Tunable phase plate made from dielectric elastomer actuator. (a) Applying a voltage to the compliant carbon black electrodes compresses the polymer between the electrodes and, as a result, increases the optical path length in the clear area inside the electrode ring. (b) Phase-voltage characteristics.

to the phase plate for a more linear working range. Each phase plate is calibrated to account for variations in the fabrication procedure. For faster response time, we drive the phase plate with an undershoot pulse ($U = 0$ V) of 50-ms duration before applying the voltage corresponding to the target phase setting. After a relaxation time of 100 ms, the relative phase drift is $<0.02\ \lambda\ s^{-1}$, stable enough for TIRF-HELM imaging.

Specimen preparation

HeLa cells transfected with actin-GFP were grown on cover slips, fixed with formaldehyde and mounted in phosphate buffered saline (PBS). Fluorescent microspheres of nominal diameter 50 nm (Polyscience, Inc., Warrington, PA) were suspended 1:400 in UHQ water. The solution was (1) mixed with 1% Agarose and mounted between two cover slips or (2) dropped on a cover slip, air dried and re-wetted with water.

Image acquisition

The field of illumination was adjusted to 50 μm in diameter. In experiments with fixed illumination angle, the period of the standing wave was $\Lambda = 175$ nm, corresponding to a theoretical penetration depth of the evanescent field of $d = 92$ nm. Each acquired data set comprised a calibration image of the illumination pattern imaged with a neutral density filter and without the dichromatic mirror, and five fluorescence images for the different phase settings of the illumination pattern. The sum of these five images will be referred to as conventional image. Total acquisition times were 0.9 s for microsphere specimens and 1.6 s for HeLa cells due to lower fluorescence signal.

Image processing

We determined the precise period and orientation of the excitation pattern from the recorded calibration image. This calibration step was performed whenever a different illumination angle was set. The five fluorescence images were background subtracted and normalized for the reconstruction. Image spectra were compensated by the measured optical transfer function (OTF) of the microscope. Noise amplification was avoided by employing a Wiener filter (Kassam & Lim, 1977) for deconvolution. The additive constant c for the filter is inversely proportional to the signal-to-noise ratio (SNR). We estimated c from the radial mean value of the spectrum divided by its variance $c = \langle \Phi(|k|) \rangle / Var[\Phi(|k|)]$ in the noise regime outside of the OTF support. Images without this OTF compensation will be referred to as unfiltered images. If c is chosen too small, noise will corrupt the separated spectra with an artefactual peak related to the spatial frequency of the grid pattern. As a result, a grid-like pattern will be superimposed on the final image. To separate the individual spectral components, we solved the linear equation system for each pixel by inverse matrix multiplication. The spectra were shifted back to the origin of frequency space by applying the Fourier shift theorem in real space. The initial phases of the illumination pattern were determined by analyzing the overlap regions of the different spectral components. To this end, we iteratively maximized the correlation coefficient between the complex angles of a finite pixel field. This method minimizes deviations introduced by single amplified noise values. In a next step, all spectral components were superimposed into a single data set to form the extended HELM passband.

The sharp edges of the extended passband were smoothed with a function providing constant weighting for regions with high SNR and apodization in a band at the edge of the spectrum. The base of this function was the OTF of TIRF-HELM T (Fig. 4(a)) modelled with an analytical OTF according to Agard (1984) for ease of scaling the base dimensions. Dividing T by itself plus a small constant $c_T \ll 1$, generated a step function $\theta = T/(T + c_T)$ of the same base dimensions (Fig. 4(b)). Next, we shrunk θ by 30% and convolved it with a circular Gaussian function. The width of the Gaussian was set to damp the spectrum down to 0.5% at the limit of the TIRF-HELM OTF. The resulting apodization function θ_{Ap} is shown in Fig. 4(c). The final TIRF-HELM image was obtained after re-sampling the pixel size from 64 to 16 nm by zero padding of the spectrum and retransforming the data into real space.

Results

We first evaluated the performance of our TIRF-HELM set-up on a water-wetted preparation of 50-nm fluorescent microspheres. Figures 5(a) and (b) clearly reveal the level of detail accessible with our 2D structured illumination that does

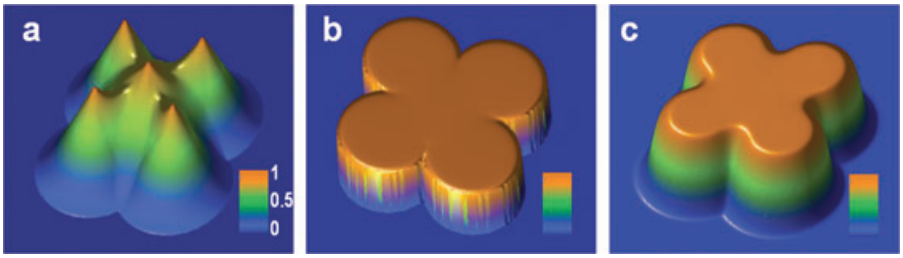

Fig. 4. Construction of an apodization function for the extended image spectrum. An analytical model (a) of the extended HELM-OTF, assembled from five standard OTFs, serves as base for the intermediate step function θ (b). Convolution with a circular Gaussian results in the final apodization function θ_{Ap} (c).

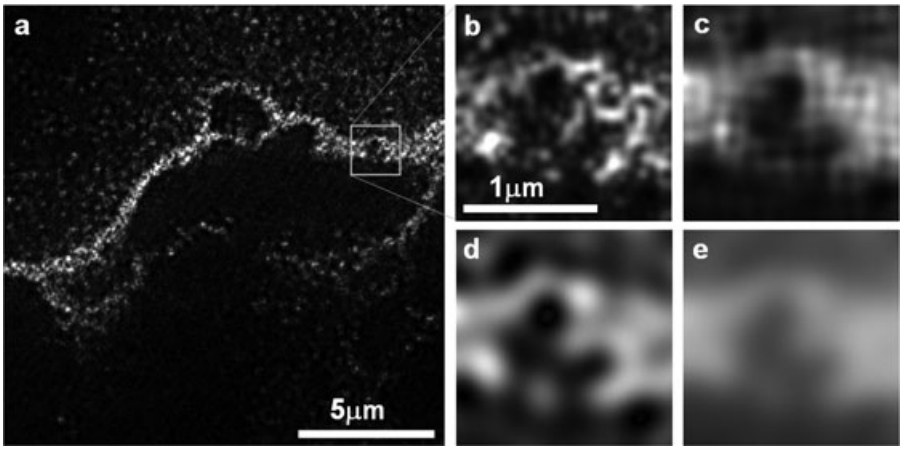

Fig. 5. (a) Fifty-nanometre-diameter fluorescent microspheres imaged by TIRF-HELM with an illumination pattern period of $\Lambda = 175$ nm. (b–e) Effect of imaging mode and data processing on image resolution, shown for the area marked in (a): TIRF-HELM with OTF-compensation and apodization function as described in text (b) and without (c); conventional TIRF image with OTF-filtering (d) and without (e).

neither require the specimen to be rotated nor any other optical or mechanical component. Comparison with the unfiltered TIRF-HELM image (Fig. 5c) demonstrates the importance of first compensating the five raw images by the microscope's OTF before reconstructing the extended HELM spectrum. The unfiltered TIRF—HELM image suffers from strong artefacts induced by the anisotropic point-spread-function (PSF) shown in Fig. 6(c). For reference, we include the conventional TIRF image, filtered with the measured OTF of the microscope (Fig. 5(d)) and unfiltered (Fig. 5(e)).

To quantify the resolution of our TIRF-HELM system, we evaluated the effective PSF obtained from 50-nm microspheres. To this end, we aligned and averaged the intensity profiles of 20 isolated beads and determined the full width at half maximum (FWHM) of the resulting signal. Figures 6(a) and (b) illustrate the PSF of conventional unfiltered TIRF microscopy and the reduction in FWHM upon filtering with the microscope's OTF, respectively. The PSF obtained for the unfiltered TIRF-HELM reconstruction (Fig. 6(c)) exhibits pronounced sidelobes in x- and y direction resulting from the maxima in the extended spectrum (cf. Fig. 4(a)). Filtering the five raw images with the microscope's OTF before reconstructing the extended resolution image effectively removes the sidelobes (Fig. 6(d)). Figure 6(e) displays cross sections through the filtered PSFs. For conventional TIRF microscopy (dashed line), we obtain an FWHM of 231 nm, whereas for TIRF-HELM (full line), the FWHM is reduced to 89 nm, which is an improvement by a factor of 2.6.

The tunable grating affords continuous control of the illumination angle without mechanical readjustment of the set-up. Hence, the penetration depth of the evanescent wave can be easily changed as documented in Fig. 7 on agarose-embedded microspheres. The penetrations depths indicated correspond to the theoretical predictions for the illumination angles used at the glass–water interface. Angles were determined from the period of the recorded standing wave illumination pattern.

To further explore the potential of TIRF-HELM on biological specimens, we recorded 1024 × 1024 pixel images of HeLa cells transfected with actin-GFP. The comparison between conventional TIRF microscopy (Figs. 8(a) & (b)) and

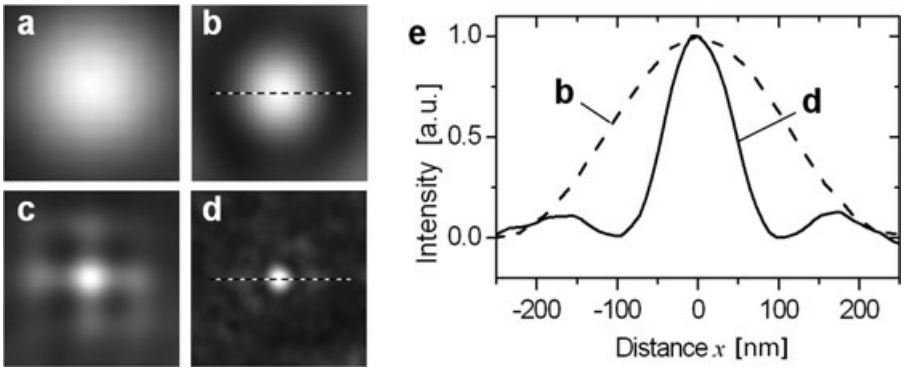

Fig. 6. Effective point spread function obtained from 50-nm fluorescent beads. Conventional TIRF without (a) and with (b) OTF-filtering; TIRF-HELM without (c) and with (d) OTF-compensation and apodization as described in the text. (e) Intensity plot along the dashed lines in (b) and (d). The FWHM of TIRF-HELM and conventional TIRF are 89 and 232 nm, respectively. Image size in (a–d) is 0.58 × 0.58 μm.

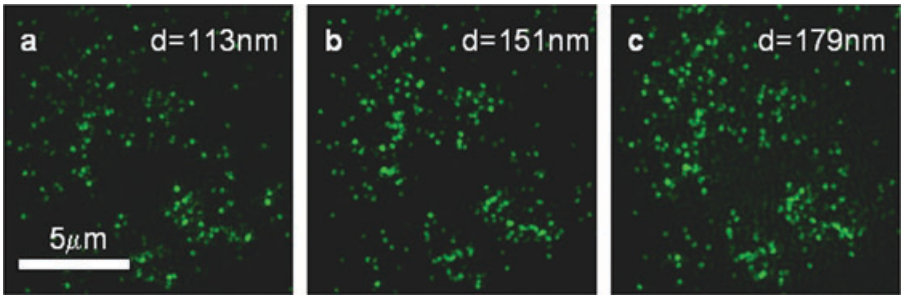

Fig. 7. Controlling the penetration depth of the evanescent wave by tuning the period of the diffraction grating. TIRF-HELM images of 50-nm fluorescent microspheres in 1% agarose. Period Λ of the standing wave illumination pattern: (a) 177.7 nm, (b) 178.2 nm, (c) 180.1 nm.

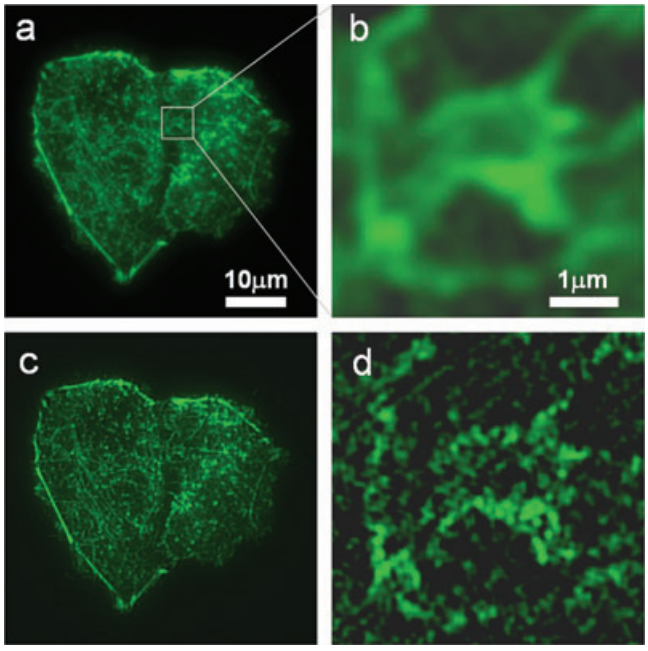

Fig. 8. HeLa cells transfected with actin-GFP (green fluorescent protein) imaged by conventional TIRF microscopy (a, b) and TIRF-HELM (c, d).

TIRF-HELM (Figs 8(c) & (d)) clearly reveals the dramatic increase in resolution achievable with structured illumination.

Conclusion

We presented a novel objective launched TIRF-HELM set-up, based on optical elements tuned by dielectric elastomer actuators. For the first time, we introduce these inexpensive polymeric optical elements in light microscopy, demonstrating their versatile properties for optical applications. The electrically tunable diffraction grating and phase shifters accomplish complete control over the illumination pattern such that no mechanical adjustments are necessary during image acquisition. In addition to setting the penetration depth of the evanescent wave, the tunable grating also allows one to easily adjust TIRF conditions for samples with varying effective refractive index. The telecentric set-up with the tunable diffraction grating placed in a secondary image plane requires few adjustment parameters and results in very low drift rates (8.3 nm min^{-1}) of the illumination pattern, making feedback control redundant. Light coupling via an aperture slider port also maintains the full functionality of the microscope.

Our image-processing algorithm allows robust determination of the absolute phase of the illumination pattern and includes an improved apodization function for the extended image spectrum. The resulting TIRF-HELM images exhibit a lateral point resolution of 89 nm.

Acknowledgements

We are grateful to R. Fiolka for stimulating discussions and computational support, and to Dr. A. Vonderheit for preparing the biological samples.

References

Agard, D.A. (1984) Optical sectioning microscopy: cellular architecture in three dimensions. *Annu. Rev. Biophys. Bioeng.* **13**, 191–219.

Aschwanden, M., Beck, M. & Stemmer, A. (2007) Diffractive transmission grating tuned by dielectric elastomer actuators. *IEEE Photonics Technol. Lett.* **19**, 1090–1092.

Axelrod, D. (2001) Total internal reflection fluorescence microscopy in cell biology. *Traffic* **2**, 764–774.

Bailey, B., Farkas, B.D.L., Taylor, D.L. & Lanni, F. (1993) Enhancement of axial resolution in fluorescence microscopy by standing-wave excitation. *Nature (London)* **366**, 44–48.

Chung, E., Kim, D., Cui, Y., Kim, Y. & So, P.T.C. (2007) Two-dimensional standing wave total internal reflection fluorescence microscopy: superresolution imaging of single molecular and biological specimen. *Biophys. J.* **93**, 1747–1457.

Chung, E., Kim, D. & So, P.T.C. (2006) Extended resolution wide-field optical imaging: objective-launched standing wave total internal reflection fluorescence microscopy. *Opt. Lett.* **31**, 945–947.

Cragg, G.E. & So, P.T.C. (2000) Lateral resolution enhancement with standing evanescent waves. *Opt. Lett.* **25**, 46–48.

Frohn, J.T., Knapp, H.F. & Stemmer, A. (2000) True optical resolution beyond the Rayleigh limit achieved by standing wave illumination. *PNAS* **97**, 7232–7236.

Garini, Y., Vermolen, B.J. & Young, I.T. (2005) From micro to nano: recent advances in high-resolution microscopy. *Curr. Opin. Biotech.* **16**, 3–12.

Gustafsson, M.G.L. (1999) Extended resolution fluorescence microscopy. *Curr. Opin. Struct. Biol.* **9**, 627–634.

Gustafsson, M.G.L. (2000) Surpassing the lateral resolution limit by a factor of two using structured illumination microscopy. *J. Microsc.* **198**, 82–87.

Gustafsson, M.G.L. (2005) Nonlinear structured-illumination microscopy: wide-field fluorescence imaging with theoretically unlimited resolution. *PNAS* **102**, 13081–13086.

Heintzmann, R. & Cremer, C. (1999) Laterally modulated excitation microscopy: improvement of resolution by using a diffraction grating. *Proc. SPIE* **3568**, 185–196.

Heintzmann, R., Jovin, T.M. & Cremer, C. (2002) Saturated patterned excitation microscopy – a concept for optical resolution improvement. *J. Opt. Soc. Am. A* **19**, 1599–1609.

Inoué, S. & Kubota, H. (1958) Diffraction anomaly in polarizing microscopes. *Nature (London)* **182**, 1725–1726.

Kassam, S.A. & Lim, T.L. (1977) Robust Wiener filters. *Franklin Inst. J.* **304**, 171–185.

Lukosz, W. & Marchand, M. (1963) Optische Abbildung unter Überschreitung der beugungsbedingten Auflösungsgrenze. *J. Mod. Opt.* **10**, 241–255.

Self, S.A. (1983) Focusing of spherical Gaussian beams. *Appl. Opt.* **22**, 658–661.

So, P.T.C., Kwon, H.S. & Dong, C.Y. (2001) Resolution enhancement in standing-wave total internal reflection microscopy: a point-spread-function engineering approach. *J. Opt. Soc. Am. A* **18**, 2833–2845.

Stephens, D.J. & Allan, V.J. (2003) Light microscopy techniques for live cell imaging. *Science* **300**(5616), 82–86.

Taylor, D.L. & Wang, Y. (1980) Fluorescently labelled molecules as probe of the structure and function of living cells. *Nature* **284**, 405–410.

